Understanding the Lunar Nearside–Farside Dichotomy via In Situ Trace Element Measurements: The Scientific Framework of a Prospective Landed Mission

Benjamin Farcy[1] , Ricardo Arevalo, Jr.[1] , and William F. McDonough[1,2,3]
[1] Department of Geology, University of Maryland, College Park, MD 20742, USA; bfarcy@terpmail.umd.edu
[2] Department of Earth Science, Graduate School of Science, Tohoku University, Sendai, Miyagi 980-8578, Japan
[3] Research Center for Neutrino Science, Tohoku University, Sendai, Miyagi 980-8578, Japan
Received 2020 October 31; revised 2021 March 9; accepted 2021 March 12; published 2021 April 28

Abstract

Trace elements, distinguished by their low abundances (parts per million by weight (ppmw)), track local, regional, and planetary-scale processes in samples sourced from throughout the solar system. Such analyses of lunar samples have provided insights on its surface rocks and interpretations of its deep interior. However, returned samples, sourced from the lunar nearside, cannot be used to address processes responsible for the morphological dichotomy between the lunar nearside and farside. The hemispherical dichotomy points to distinct evolutionary histories of these two domains, rendering our understanding of lunar history incomplete. We outline the scientific justification for a landed, in situ investigation of lunar farside lithologies, focusing on chemical analyses that will constrain the Moon's bi-hemispherical chemical evolution. Newly developed and heritage spaceflight instruments, capable of measuring low element abundances (limits of detection <10 ppmw $\pm 20\%$), can be deployed on the lunar farside and provide constraints on (1) the temperature and pressure of mare basalt crystallization, (2) depth-dependent mineralogical and compositional changes in the lunar mantle, (3) the chronology of major geologic events, and (4) abundances and distributions of refractory and heat-producing elements of the lunar farside mantle. The science return and logistical challenges of targeting four specific landing sites on the lunar farside are identified: Moscoviense, Apollo, Von Kármán, and Leibnitz craters. These sites maximize impact melt basin lithologies and later mare magmatism, and they minimize terrain hazards.

Unified Astronomy Thesaurus concepts: Earth-moon system (436); Mantle (1005)

1. Introduction

The chemistry of the Moon holds the key to understanding the early history of the Earth–Moon system, as well as the sequence of formative events in the timelines of other planetary objects. In particular, the composition of the lunar interior provides a window into the chemical and isotopic fractionation provoked by the Moon-forming event. The Moon's surface additionally informs on the dynamics of lunar differentiation, calibrates crater counting chronologies, and provides access to mission-enabling resources. Thus, exploration of the lunar crust and mantle-derived materials is important to constraining the evolution of the Earth–Moon system and supporting human exploration objectives. The Planetary Science Decadal Survey 2013–2022 (NRC, 2011) and Lunar Exploration Roadmap (LEAG, 2016) highlight the need to characterize the stratigraphy and structure of the Moon as a means to resolve the initial conditions of solar system formation and inform on the accretion, differentiation, and impact history of the inner planets.

The bulk composition of the inner solar system can be described to >90% with only four elements, namely, Fe, O, Mg, and Si, which govern the primary mineralogies of these bodies. In contrast, trace element abundances (<1000 parts per million by weight (ppmw)) do not determine sample mineralogy; rather, the abundances and distributions of trace elements are controlled by mineral-melt partitioning behaviors that reflect the temperature, pressure, and redox conditions of the system. Consequently, trace element abundances can vary by orders of magnitude in cogenetic

geological samples and serve as sensitive tracers of planetary processes.

Here we provide details of a potential lunar landed mission that can deliver key chemical and isotopic information, giving insights into lunar stratigraphy, chronology, and differentiation. We outline the scientific justification for such a mission in which heritage or developing spaceflight analytical techniques can be used to determine the absolute and relative abundances of a wide range of trace elements and isotopic systems. Our landing site recommendations focus on lunar farside targets, as these would be best suited to deliver the greatest scientific return.

2. Science Objectives

The morphological and lithological dichotomy between the lunar nearside and farside is well documented (Kaula et al. 1974; Head & Wilson 1992; Jolliff et al. 2000; Shearer et al. 2006; Ohtake et al. 2012), implying distinct formational histories of the crust and mantle of each hemisphere. Further constraints are needed to understand better the composition and formational history of the lunar farside, and thus the Moon. Models explaining the crystallization sequence of the Lunar Magma Ocean (LMO) depend on accurate predictions of the temperature and composition of the crystallizing liquid, and there are robust constraints from nearside sampling, but little information for the farside. Here, we identify measurements that will constrain (1) the temperature and pressure of formation of farside mare basalts, (2) the mineralogical composition of the lunar farside mantle, (3) the chronology of major geologic events in the Moon's past, and (4) the refractory element enrichment and volatile element depletion of the bulk Moon relative to Earth (see Figure 1). We seek to enhance orbital-
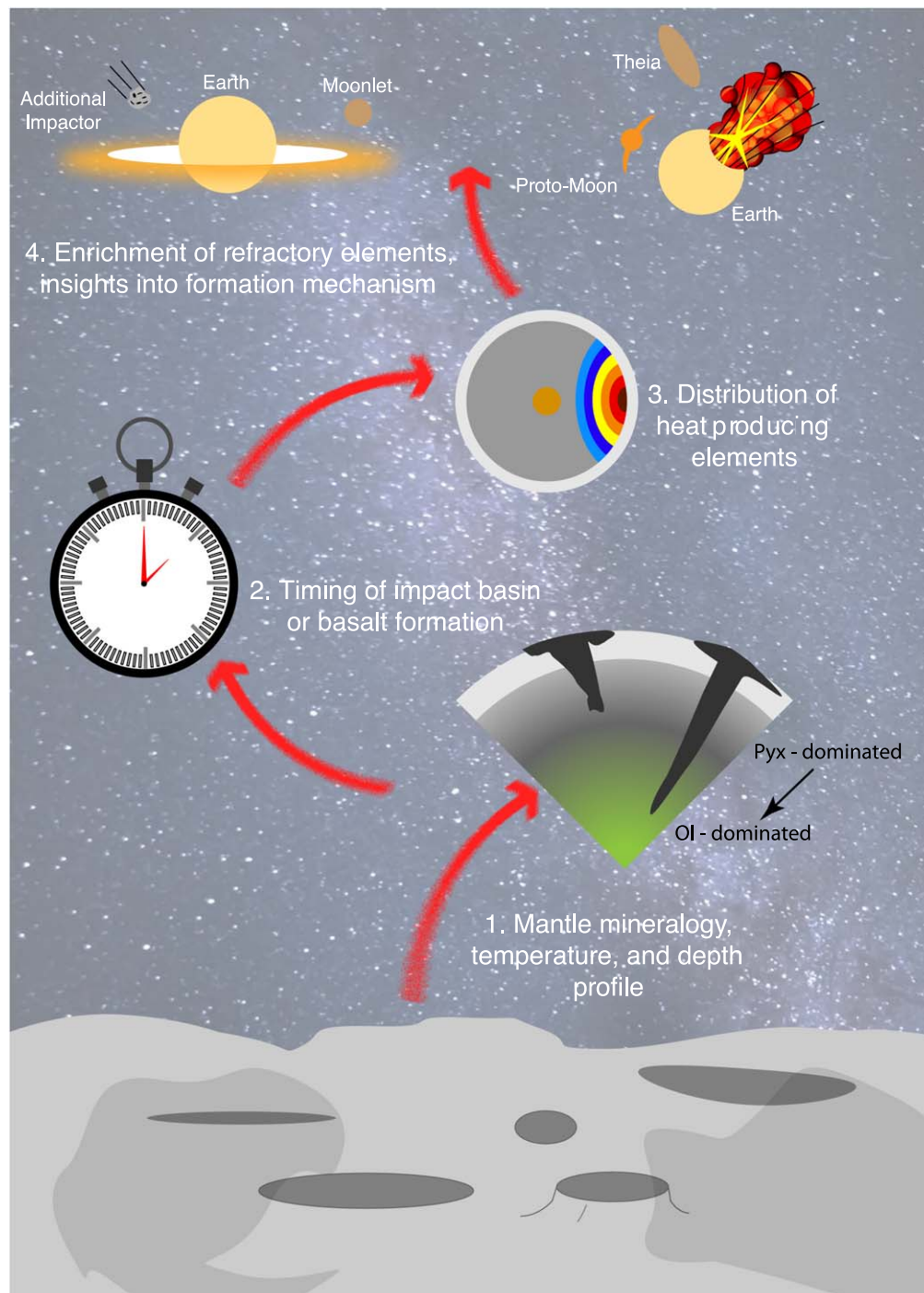
Figure 1. Cartoon diagram of science objectives for a landed farside lunar mission, with a focus on trace element geochemistry. Measurements of FRTE ratios and partition coefficients of temperature- and pressure-sensitive elements (e.g., Ni) between mineral phases in basaltic melts can provide insight into the formation history and composition of the farside mantle source region. K-Ar and Rb-Sr radiometric systems can then be used to estimate the timing of mare basalt emplacement and impact melt events. Determining refractory element abundances of impact melts will help constrain the farside mantle abundance of HPEs, giving insight into the thermal evolution of the lunar farside and formation mechanisms of the Moon.

based measurements, carried out on a regional scale, with in situ data for specific lunar settings and lithologies. Hemispherical source locations of lunar meteorites are not well established, and return samples from Apollo and Luna missions access only the nearside, biasing our view of lunar evolution. Taken together, the four science objectives described here will help define the temperature-dependent crystallization sequence of the LMO for farside mantle material and provide further compositional and temporal constraints for its subsequent melt products. An overview

of the proposed analyses and the elements targeted can be found at Table 1.

2.1. Temperature and Pressure of Mare Basalt Formation

Crystallization of the LMO leads to a characteristic stratigraphy of cumulate mineralogy, defining a bottom-up petrologic evolution to the lunar mantle (Wood et al. 1970; Snyder et al. 1992; Elkins-Tanton et al. 2011; Charlier et al. 2018; Rapp & Draper 2018).

Table 1
Summary of Elements, Geologic Phases, and Abundances Targeted for Trace Element Analysis in the Investigations Prioritized Here

|	Thermobarometry	Source Mineralogy	Chronology	Refractory/Volatile + HPEs[*]
Elements to be measured	Al, Cr, Ni, Mg, Ti, Na	Ca, Ni, Co, Mn, Fe, Zn, Ga, Ge	K, Ar, Rb, Sr	K[*], Th[*], U[*], Al, Ca, Zn, Li
Minerals targeted for analyses	Olivine, clinopyroxene, ± spinel oxide	Olivine, clinopyroxene, orthopyroxene, bulk rock	Bulk rock, multiple phases	Bulk Rock
Range of abundances	10^1 ppm (Al in olivine) to wt.% (Mg)	10^2 ppbw (Ge) to 10^3 ppmw (Ni)	10^1–10^2 ppmw (Rb + Sr) to wt.% (K)	10^2–10^3 ppb (Th and U) to wt.% (K, Al, Ca)
Landing site lithology targeted	Basalt flow	Basalt flow	Impact melt, basalt flow	Impact melt
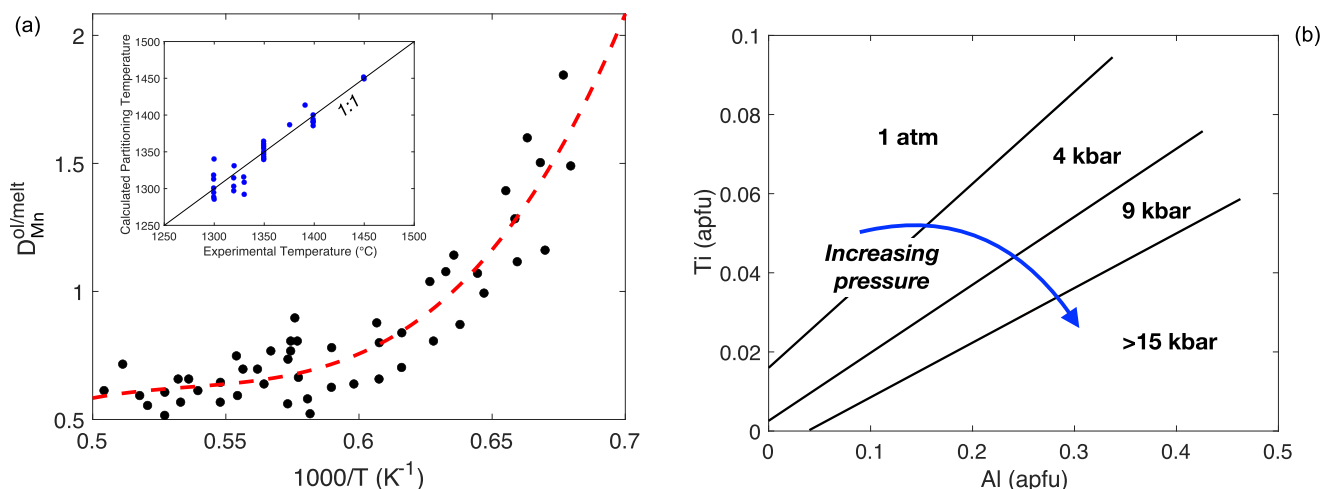
Figure 2. (a) Example of calibrated geothermometer, using the temperature-sensitive partitioning of Mn between olivine and melt during controlled melting experiments. In situ measurements of mineral and matrix can be used to estimate the temperature of melting. Inset shows calibration between controlled experimental temperature and that derived from a partitioning-based geothermometer. Figure modified from Davis et al. (2013), with inset figure modified from Wan et al. (2008). (b) Geobarometer calibrated using pressure-sensitive partitioning of Al and Ti in clinopyroxene, calibrated via controlled high-pressure experiments from Nekvasil et al. (2004). Measurements of Al and Ti in pyroxene from mare basalts can constrain the depth of mantle melting. Al and Ti abundances as atoms per formula unit (apfu).

While the temperature of the LMO melt controls the crystallizing sequence, uncertainty remains regarding the distribution of radiogenic heat during early lunar differentiation, and thus the temperature distribution throughout the early Moon. The Moon possibly formed with an asymmetric distribution of heat-producing elements (HPEs; Garrick-Bethell et al. 2010; Laneuville et al. 2013, 2018), which would lead to a different crystallization sequence on the lunar farside (Elardo et al. 2020). However, this interpretation is not supported by spectroscopic surveys of the South Pole Aitken (SPA) basin, where an HPE-rich layer has been identified under the lunar farside that was excavated through impacts (Jafar & Pentecost 2001; Hagerty et al. 2011; Evans 2019; Moriarty et al. 2020). Because of this potential for thermal asymmetry, the temperatures and pressures at which mare basalts melt and crystallize may be different for farside and nearside basalts. Petrologic differences between melt products from the two hemispheres may exist. Here, we outline analyses that will help constrain the petrogenesis of farside mare basalt in order to better understand its mantle distribution of heat.

Estimates of the depth and temperature of source region melting are based on analyses of returned mare basalts and picritic glasses, both of which are derived from isotopically distinct source regions (Tatsumoto et al. 1973, 1987). Whereas mare sources are modeled with minimum melting depths of 100–250 km (Longhi 1992), picritic glasses indicate melting depths from 360 to 520 km in a garnet-bearing lithology, possibly forming below the depth of LMO cumulate formation, sampling primitive unmelted lunar mantle material (Shirley & Wasson 1982; Delano 1986; Longhi 1992, 1993; Neal 2001). Picritic glasses also likely formed at greater temperature, estimated at 1410°C–1500°C, as compared to 1200°C–1380°C for mare basalts (Longhi 1992, 1995). Despite constraints on the temperature and pressure of melt generation from the lunar nearside, similar estimates are lacking for the farside. Temperature and pressure estimates from farside mare basalts can help constrain their mantle solidi, and by extension farside mineralogy and petrology, enabling comparisons to compositional models of the lunar nearside. Key measurements

of trace element abundances can provide an indirect gauge of the temperature profile of the lunar farside mantle.

Crystallization temperatures and pressures can be inferred through the observed distribution of trace elements between two (or more) phases, calculated as $D_X^{phase1/phase2} = \frac{C_1}{C_2}$, where $D_X^{phase1/phase2}$ is the partition coefficient of element X, which is sensitive to temperature and/or pressure, and C_1 and C_2 are the element concentration in each phase. Geothermometers are commonly calibrated via controlled high-temperature and high-pressure melting experiments, in which synthetic oxide mixtures or natural basalts are melted at varying temperatures and the partitioning of temperature-sensitive elements is measured between phases as a function of experimental temperature. For example, the temperature-sensitive partitionings of Al and Cr between olivine, Cr-spinel, and melt (De Hoog et al. 2010; Coogan et al. 2014), Mg# in olivine (Herzberg & Asimow 2015), Ni between olivine and melt, (Roeder & Emslie 1970; Wang & Gaetani 2008), and Na_2O between clinopyroxene and melt (Putirka 1999; Putirka et al. 2007) have all been used as indirect gauges of crystallization or equilibration temperature (Figure 2(a)). These thermometers can be applied to a variety of mantle-derived lithologies (e.g., kimberlites, mantle xenoliths, and basaltic mantle melts) from across a range of compositions and temperatures.

Measurements of crystallization pressure can produce a depth profile of lunar mantle melting, revealing changes in composition and temperature as a function of depth. Pyroxene can serve as an example of a geobarometer and can be used to infer local pressure of melt systems. As elements with "3+" cation charges substitute for "2+" cations in the M1 site of a mineral, lattice strain theory predicts that this site becomes smaller at high pressure. Al is more likely to be accepted into the mineral than Ti owing to its smaller ionic radius ($Al^{3+} = 67.5$ pm, $Ti^{3+} = 81$ pm), thereby allowing less Ti into the site and lowering the Ti/Al ratio at higher pressure. Thus, the Ti/Al ratio in pyroxenes can be used to measure the pressure of sample crystallization. This barometer has been calibrated by Nekvasil et al. (2004) and Filiberto et al. (2010)
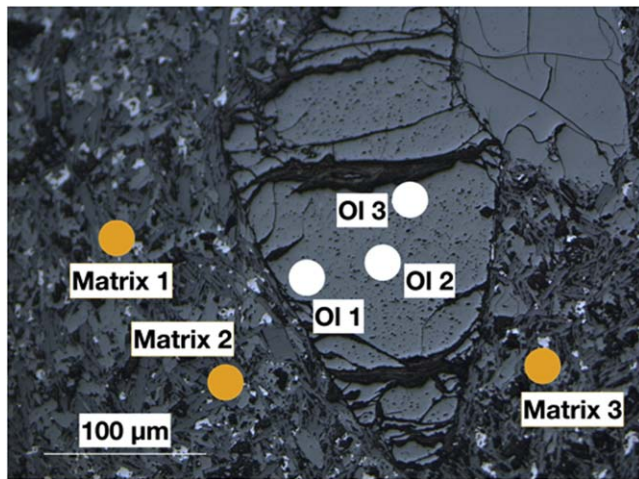
Figure 3. Olivine phenocryst in fine-grained matrix in basalt from St. Helena island. White and orange dots show example measurement spots needed to calculate partitioning ($D_X^{ol/melt}$) value. Photo taken using JEOL 8900R electron probe microanalyzer at the University of Maryland, College Park.

Figure 4. Example of FRTE ratios being used to estimate mantle source composition. The yellow area represents the range of values for OIBs. Figure modified from Le Roux et al. (2011).

from atmospheric pressure to >1.5 GPa (Figure 2(b)) and applied to Martian shergottites (Nekvasil et al. 2007; Combs et al. 2019).

Trace elements targeted for this investigation occur over a range of abundances in lunar and terrestrial rocks, so instrumentation with a large dynamic range is needed to carry out these analyses. For Earth, the range of olivine-mineral equilibration temperatures produces olivine Al and Cr abundances of tens of ppmw. This is in contrast to the more efficient partitioning of Ni in olivine, which can yield concentrations as high as 3500 ppmw (Sobolev et al. 2005), although lunar bulk rock and olivine Ni abundances are typically <200 and <600 ppmw, respectively (Shearer & Papike 2005; Longhi et al. 2010). An in situ analysis would require measurements of specific trace elements (e.g., Ni, Cr, or Al) in multiple phases in the sample (e.g., Figure 3). Therefore, spaceflight instrumentation designed for trace element measurement with a range of limits of detection and high-resolution optical cameras for mineral-specific analyses could provide access to these proxies.

2.2. Lunar Mantle Mineralogy

Trace element systematics of returned lunar basalts and glasses help constrain the mineralogy and composition of the lunar nearside mantle. The LMO crystallization sequence produced a stratigraphy of cumulate ultramafic minerals and oxides in the lunar mantle, which likely underwent restructuring due to mantle overturn caused by the accumulation of dense oxide material (Solomon & Longhi 1977; Warren 1985; Hess & Parmentier 1995; Boukaré et al. 2018). Samples of nearside mare basalts and glasses show a mantle source that is likely pyroxenitic to lherzolitic in composition, with composition becoming more mafic with increasing depth. Heavy rare earth elements (REE) abundances in picritic glasses also indicate the possibility of sampling undifferentiated, garnet-bearing "primitive" lunar material (Neal 2001) at greater depth. The change in mantle composition as a function of depth is further supported by geophysical evidence from the Apollo seismic network, which indicates a pyroxene-dominated upper mantle from 238 to 488 km and an olivine-dominated lower mantle
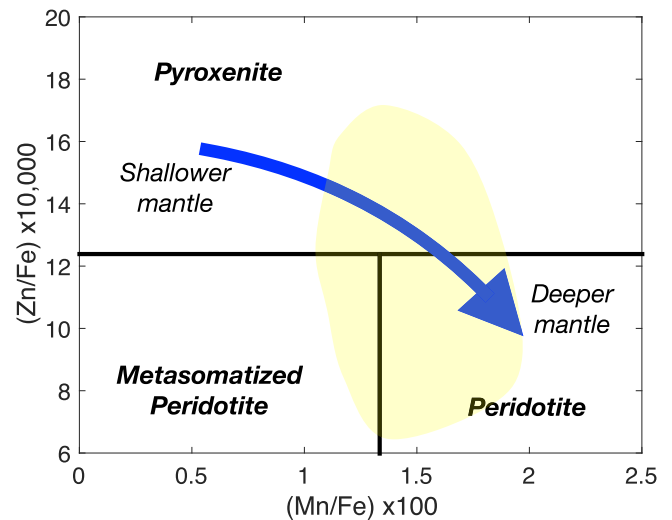
<488 km, with increasing Mg# with depth (Kuskov & Kronrod 1998; Gagnepain-Beyneix et al. 2006).

The trace element content of the mantle source regions reveals the extent of chemical processing as well. Low-Ti basalts are depleted in incompatible elements and contain chondritic ratios of refractory elements (e.g., Zr/Hf, Nb/Ta), while high-Ti basalts contain nonchondritic ratios and incompatible element enrichments (Neal 2001). This indicates that source differentiation likely led to separate chondritic and nonchondritic mantle sources (Wieczorek et al. 2006). But while the composition of mare and picritic glasses provides constraints on their respective source regions, similar constraints for the lunar farside mantle are needed. If the lunar mantle cumulate overturn was caused by the buildup of high-density oxide phases, and an asymmetric distribution of heat caused a heterogeneous mantle crystallization, then the cumulate overturn event may have proceeded differently on the farside compared to the nearside (Zhong et al. 2000; Parmentier et al. 2002; Laneuville et al. 2018).

During mantle melting, certain trace element ratios fractionate little relative to each other owing to their similar partition coefficients, and instead retain the trace element ratios of the mantle sources. For example, concentrations and ratios of first row transition elements (FRTEs) in mantle-derived materials (e.g., basalts) can be used to infer the ratio of olivine to pyroxene in their respective mantle sources (Le Roux et al. 2011). For Earth, whole rock Ni/Co ratios <6 indicate a pyroxenitic mantle source, while Zn/Fe (×10,000) ratios <12 and Mn/Fe (×100) ratios >1.4 indicate melting of peridotite sources (Figure 4). In addition to whole rock abundances, source lithology can further be inferred using FRTE ratios in specific minerals (e.g., olivine, pyroxenes). Ni, Mn, and Ca partitioning between olivine is controlled by the extent of peridotite or pyroxenite melting and correlates with long-lived radiogenic isotopes (e.g., Sr, Nd, Pb; Gurenko et al. 2009; Matzen et al. 2017). Ratios of Ge to FRTEs or other elements can be an important indicator of source composition, due to the different partitioning behavior of Ge between peridotite and pyroxenite during partial melting ($D_{Ge}^{ol/melt} = 0.42$, $D_{Ge}^{cpx/melt} = 0.87$; Davis et al. 2013; He et al. 2019). Analysis of mid-ocean ridge basalt (MORB) and ocean island basalt (OIB) samples suggests that Ge/Si ratios

$>7.5 \times 10^{-6}$ are common for peridotite mantle sources with minimal pyroxenitic influence, while ratios $<6 \times 10^{-6}$ are indicative of the addition of pyroxenite to the mantle source (Yang et al. 2020). Ge can also be leveraged as an indicator of source lithology using the Ga/Ge ratio, as differences in this ratio are observed between MORB and Hawaiian OIB, reflecting differences in mantle source composition. Ge is also an indicator of mantle metasomatism in the Moon, as higher abundances of Ge are typically found in conjunction with fluid-mobile volatile elements (Dickinson et al. 1989).

Measurements of FRTE ratios, such as Zn/Fe, Mn/Fe, Co/Fe, or Ni/Co, as well as Ge/Si or Ga/Ge, can deliver insight into the relative proportion of peridotite and pyroxenite in the farside mantle. The FRTEs discussed here occur in lunar basalts in abundances of 1 ppmw to hundreds of ppmw, although Ge ranges from 1 ppbw to 1 ppmw (Wolf & Anders 1980), which could prove challenging for future analyses. While the framework to determine source composition through FRTE ratios has been established for the terrestrial mantle, further modeling and empirical observations are required to apply these ratios to lunar samples. For example, the Zn/Fe ($\times 10,000$) ratio typically ranges from 4 to 20 in MORB samples, while this ratio is typically <1 in lunar mare basalts, likely due to the volatile depletion of Zn in the bulk silicate Moon (BSM). Regardless, these proxies can be leveraged to estimate lunar mantle mineralogy from common surficial mare basalt flows.

The analyses proposed here, in conjunction with estimates of pressure and temperature, will act as a petrologic cross section of the lunar mantle, revealing changes in lunar farside mantle composition with depth. Farside mare basalts that are sourced from varying depth in the lunar mantle could represent different cumulate stratigraphies as their source regions. Thus, trace element constraints on depth of mare basalt formation, coupled with estimates of the source mineralogy at that depth, could provide insight into the depth profile of the lunar farside mantle and its contrast to the nearside mantle.

2.3. Chronology

Chronology of major geologic events throughout the solar system is a critical aspect of our understanding of planetary formation, history, and evolution. Significant effort has been employed to constrain the timing of major events in lunar history, such as the initial formation of the Moon, LMO crystallization and differentiation, and the history of impact cratering. Chronological constraints have traditionally been placed on these events by radiometric age determination via long-lived radioisotopes (e.g., Rb-Sr, U-Pb, Sm-Nd, K-Ar) in returned samples and meteorites, or by crater counting statistics. However, sampling bias from the nearside and large uncertainties associated with crater counting models make accurate timing of global lunar events difficult.

Constraints on early lunar history are derived from the chronology of returned lunar material. U-Pb and Hf-W isotope systematics of lunar and terrestrial samples indicate a Moon-forming impact age of 4.50–4.51 Ga, implying early lunar formation (Barboni et al. 2017; Thiemens et al. 2019; Maltese & Mezger 2020), while other estimates using U-Pb ages in zircons derived from lunar breccias place the age of the impactor later at ~4.42 Ga (Nemchin et al. 2009; Connelly & Bizzarro 2016; Maurice et al. 2020). Rb-Sr and Sm-Nd isotope systematics of samples representing the latest stages of LMO crystallization indicate that Mg-suite, ferroan anorthosite, potassium, rare earth

element, and phosphorus (KREEP) rich lithologies, and a mare basalt source formed concordantly with each other at ~4.35 Ga within a 40 Myr span, suggesting a common reservoir source for those samples (Borg & Gaffney 2015; Borg et al. 2020). These ages of late LMO crystallization are concordant with the ~4.34 Ga age determined from meteorite MIL 13317, which is possibly derived from the lunar farside (Curran et al. 2019). U-Pb age constraints have been used in conjunction with thermal models of LMO crystallization and indicate that the final 10% of highly enriched KREEP material possibly existed in its molten state for 100–200 Myr owing to an insulating anorthositic crust and high concentration of HPEs (Nemchin et al. 2009; Maurice et al. 2020). Thus, chronology of returned samples outlines the sequence of events from lunar impact origin to LMO crystallization.

The age constraints placed on returned samples via radiometric dating are critical to our understanding of lunar history, as these sample ages can be extended to other regions and stratigraphies of the Moon through crater counting statistics. Absolute model ages (AMAs) based on cratering statistics use relative ages of distinct geologic units throughout the Moon, which are subsequently constrained by radiometric ages of returned samples. However, the rate of impact flux is lacking constraints >3.9 Ga (Bottke & Norman 2017) and contains high uncertainties for the period between 1 and 3 Ga (Hartmann 2019; Cohen et al. 2021). While the landing sites proposed here do have AMA estimates for various units based on the cratering record, in situ radiometric age constraints on impact melt deposits on the lunar farside can better calibrate the crater counting statistics that AMA estimates depend on.

Despite the constraints discussed here, lunar crustal formation possibly proceeded asymmetrically between the farside and nearside owing to the thermal difference between hemispheres during LMO crystallization, leading to differences in the timing of farside crust and mantle formation. The farside crust likely crystallized first owing to the lower temperature of the farside magma ocean, forming greater amounts of anorthositic material from a more mafic melt (Arai et al. 2008). This is supported by orbital-based measurements of farside anorthosite, which is thicker (Ohtake et al. 2012; Wieczorek et al. 2013) and more Mg-rich (Ohtake et al. 2009; Crites & Lucey 2015) than the nearside. Because of the nearside sampling bias and uncertainties associated with crater counting statistics, our understanding of the chronology of farside crust and mantle crystallization, and thus of the LMO as a whole, is limited. In situ chronological measurements can provide a more complete picture of the formation of the two lunar hemispheres.

In situ geochronology can be carried out using radioactive parent/daughter isotope ratios, mainly $^{87}Rb/^{87}Sr$ and $^{40}K/^{40}Ar$. Radiometric ages provide time constraints for when samples crystallized and closed to diffusion. Specifically, K-Ar systematics are a useful tool for lunar chronometry and history, due to its sensitivity to impact events, surficial exposure, and solar wind implantation. Rb-Sr chronology is an additional tool that can provide age constraints at higher sample closure temperatures than the K-Ar system. However, a main issue in measuring these isotopes through mass spectrometry is born from the overlapping mass peak of ^{87}Rb on ^{87}Sr, or ^{40}K on ^{40}Ar. To circumvent this challenge, steps are typically taken to separate the signals from the two isotopes either by signal correction or through physical separation of the parent and daughter isotopes. The Rb-Sr and K-Ar isotope systems have been used extensively to identify

distinctions in terrestrial sources of MORB and OIBs, as well as planetary material from the Moon, Mars, and chondritic meteorites.

In situ measurements of K, Ar, Rb, and Sr in samples representing late-stage LMO cumulates could be targeted to make chronological constraints analogous to those previously discussed. Data from the Clementine and Kaguya-GRS missions show K abundances on the lunar surface as high as 1–2 wt.% in nearside mare deposits, with 600–1100 ppmw K in the South Pole Aitken (SPA) basin and 100–250 ppmw in the anorthositic highlands (Gillis et al. 2004; Zhu et al. 2011). Measurements of the $^{87}Rb/^{86}Sr$ and $^{87}Sr/^{86}Sr$ ratios are more accessible to terrestrial and spaceflight analytical techniques than other chronometers (e.g., U-Pb), as Sr abundances in typical lunar and terrestrial rocks range from tens to hundreds of ppmw as opposed to ppbw-level concentrations. However, Rb abundances in lunar rocks are typically between 1 and 40 ppmw owing to the depleted nature of moderately volatile elements in the BSM (Warren & Taylor 2014).

In addition to the previous discussion, in situ chronology on the lunar farside can provide insights into the putative period of lunar and solar system history characterized by an increase in meteoritic bombardment at ∼3.9 Ga, known as the "terminal lunar cataclysm," which would have produced a proportional increase in bombardment on Earth during the era when life began to arise (Bottke & Norman 2017). This period of solar system history, known as the late heavy bombardment (LHB), requires further age constraints for the impact formation of the SPA basin to understand better the duration and magnitude of this cataclysm event. Specifically, Rb-Sr or K-Ar isochron ages with uncertainties less than ±200 Ma (2σ) for ∼4 Ga samples would be sufficient to discriminate between an impact cataclysm at 3.9 Ga and part of the declining bombardment beginning at 4.2 Ga. A full discussion of this history is beyond the scope of this paper; for more information on in situ chronological applications for the LHB, see Cohen et al. (2021).

2.4. Refractory and Volatile Element Content of the Moon

The compositions of terrestrial planets depend on their source materials, as well as the processes associated with accretion, including (but not limited to) incomplete condensation and evaporative loss of volatile elements. Planetary formation processes in the inner solar system could have resulted in enrichments of refractory elements and depletions in moderately volatile elements (elements with half-mass condensation temperature of <1250 K at 10^2 Pa) relative to Earth. For example, the absolute and relative abundances of the HPEs provide insights, as K is volatile and Th and U are refractory. Mass balance estimates of the composition of the silicate portion of the Moon allow for a possible enrichment in refractory lithophile elements (e.g., Ca, Al, Th, U) by a factor of up to $1.5\times$ relative to the bulk silicate Earth (Morgan et al. 1978; Kuskov & Kronrod 1998; Taylor 1999; Gagnepain-Beyneix et al. 2006; Taylor et al. 2006). However, other models report terrestrial absolute abundances of refractory lithophile elements in the BSM equivalent to that in bulk silicate Earth (Wänke & Dreibus 1982; Warren 2005; Longhi 2006; Taylor & Wieczorek 2014). The Moon is depleted in volatile and moderately volatile elements (e.g., K, Li, Rb, Zn) relative to Earth, leaving even more uncertain the BSM abundances and distributions of these elements (Wolf & Anders 1980; Jones & Palme 2000; Davis 2006; Day & Moynier 2014; Canup et al. 2015). This depletion of volatiles and a potential enrichment in

reftactory elements have major implications for the lunar thermal history, with respect to the relative and absolute abundances of K, Th, and U, the HPEs.

Estimates of lunar refractory and volatile element abundances are based on analyses of returned samples, meteorites, and orbital-based measurements of the lunar surface. Due to the nearside sampling bias of returned samples and the limitations of orbital-based measurements (e.g., limits of detection, large spatial scale, sampling depth), our understanding of the relative or absolute abundances of refractory and volatile element abundances requires more constraints. Here, we discuss measurements proposed to understand better the refractory and volatile element abundances in the lunar farside mantle.

The K/U and K/Th ratios, derived from lunar samples and γ-ray spectroscopy measurements of the surface, indicate a lunar K/U of 1500–3000 (Taylor 1982; Stegman et al. 2003; Hagerty et al. 2006) and K/Th of 360–460 (Prettyman et al. 2006; Laneuville et al. 2018). This is lower than Earth's (K/U = 14,000 ± 1300, K/Th = 3,000 ± 750) and chondritic (K/U = 66,000 ± 5000, K/Th = 18,000 ± 1200) values (McDonough & Sun 1995; Arevalo et al. 2009; Farcy et al. 2020a; Lodders 2020). Fractionation of K/U, albeit slightly, is due to magmatic processing (Lassiter 2004; Arevalo et al. 2009; Arevalo & McDonough 2010; Farcy et al. 2020a). Thus, if the lunar farside mantle evolved with a different crystallization sequence than the nearside, then ratios of HPEs may be fractionated in the lunar farside mantle relative to the nearside.

In addition to the absolute abundance of HPEs in the bulk Moon, the distribution of HPEs between nearside and farside interiors may have contributed to its dichotomy. Dynamic models of the long-term evolution of lunar reservoirs suggest that uneven crystallization of the LMO and tidally driven gravitational harmonics possibly trapped HPE-rich liquid preferentially on the nearside (Garrick-Bethell et al. 2010). This asymmetry in HPE distribution would have produced over an order of magnitude more basaltic melt on the nearside relative to the farside (Laneuville et al. 2013, 2018). However, γ-ray surveys of the SPA basin show elevated Th abundances in excavated lower crustal material, indicating the presence of an HPE-rich KREEP layer underlying the lunar farside (Hagerty et al. 2011; Moriarty et al. 2020). A portion of this layer may have been redistributed to the nearside during the SPA basin impact, despite the Moon initially forming with a KREEP-rich layer on the farside (Jafar & Pentecost 2001). Thus, the distribution of HPEs between the lunar nearside and farside requires further constraints to resolve these issues. In situ analyses of HPE abundances of surficial material from basaltic flows and impact basins can provide needed information on the absolute abundance of K, Th, and U in the BSM, as well as their lateral distribution throughout the planetary interior.

Measuring the HPE relative and absolute abundances in lunar farside materials would require instrumentation capable of measuring a wide range of elemental concentrations, as the absolute abundance in lunar mantle rocks may be <10 ppbw. A landed mission would likely require the ability to measure K, Th, and U at low limits of detection and smaller spatial scales in mantle rocks exposed at the surface.

Further, analyses of HPEs should preferably be carried out on surficial deposits that are reflective of the lunar farside mantle. Specifically, large-scale impacts produce basins that expose previously molten upper mantle material to the surface.

These impact melt sheets can differentiate through fractional crystallization, concentrating incompatible elements in the final dregs of the melt and further complicating mantle estimates of HPEs (Dhingra et al. 2013; Vaughan & Head 2014). However, some impact melt basins are calculated to have continued convecting after melt generation, preventing impact melt sheet differentiation and producing material representative of a homogenized upper mantle (Cassanelli & Head 2016). Farside basins that contain norite and troctolite impact melts are thought to be representative of the lunar upper mantle and would be ideal targets for the measurements proposed here (Yamamoto et al. 2012; Moriarty et al. 2013; Hurwitz & Kring 2014; Miljković et al. 2015; Melosh et al. 2017; Moriarty & Pieters 2018).

3. Instrumentation for Chemical Analysis

Analytical techniques developed for terrestrial labs continue to be miniaturized, enabling new applications for trace element measurements for planetary exploration. Here, we provide an overview of the various techniques previously applied to major and trace element characterization of planetary environments, as well as novel developments of future in situ detection techniques.

3.1. Spaceflight-heritage Instrumentation

One of the most common analytical techniques, flown on a range of missions from the Viking landers (Biemann et al. 1977) to the Curiosity rover (Mahaffy et al. 2012) and the ExoMars Rosalind Franklin Rover (Goesmann et al. 2017), is pyrolysis gas chromatography mass spectrometry (pyr/GCMS). This method measures abundances of volatile elements and organic compounds, particularly those associated with minerals that break down at temperatures $\leqslant 900°C$ (e.g., phyllosilicates). To measure minor and trace elements specifically, the payloads of the Viking 1 and 2 landers also included X-ray fluorescence spectrometers with detection limits below 100 ppmw for select elements (e.g., Rb and Sr; Clark et al. 1977). XRF instrumentation has also characterized the composition of the surface of Venus via Venera 13 (Surkov et al. 1984) and other sites on Mars via Curiosity (Blake et al. 2012); a microXRF instrument is on board the Mars 2020 rover (Allwood et al. 2015).

The Mars Exploration Rovers, Spirit and Opportunity, incorporated miniaturized thermal emission spectrometers to characterize local mineralogy and Mossbauer spectrometers to specifically identify iron-bearing phases. To access low abundance trace elements, Spirit and Opportunity carried an Alpha Particle X-Ray Spectrometer (APXS; Rieder et al. 2003), as on Surveyors 5–7 (Patterson et al. 1969), Mars Pathfinder (Foley et al. 2001), Curiosity (Campbell 2012), and Rosetta's Philae lander (Klingelhöfer et al. 2007). The detection limits of alpha-particle scattering extend below 100 ppmw for some elements, comparable to XRF techniques.

ChemCam, a laser-induced breakdown spectrometer (LIBS) on board Curiosity, enables spatially resolved minor and trace element measurements at standoff distances up to 7 m away from the source (Wiens et al. 2012); an analogous LIBS instrument augmented to support remote Raman spectroscopy was recently launched on board the Mars 2020 rover (Wiens et al. 2017). Such LIBS techniques promise detection limits as low as <100 ppmw for many alkali and alkaline Earth metals (Wiens et al. 2013). On board the Rosalind Franklin rover, the
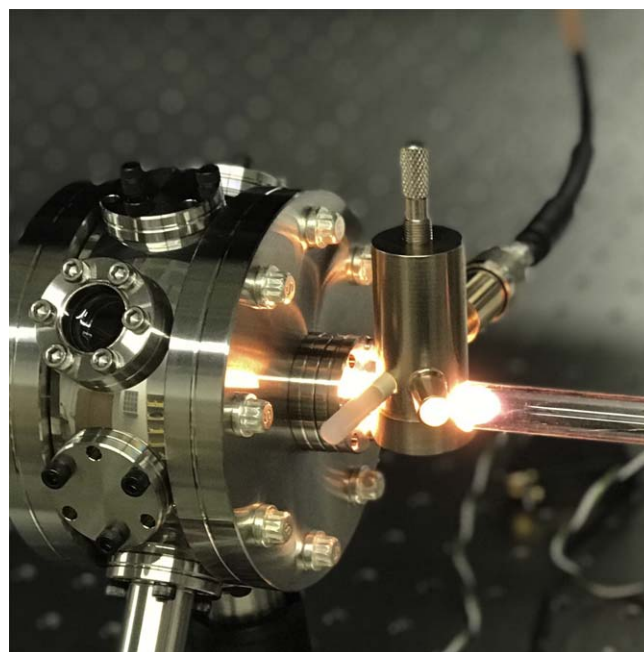

Figure 5. Photo of a low-power He plasma source, generated with 14 W of power and 200 mL min^{-1} gas, developed at the University of Maryland, College Park.

MOMA instrument's laser desorption/ionization mode can also determine the elemental chemistry of Martian materials with fine spatial resolution, but analyses are limited to samples that are physically collected by the rover, and detection limits have yet to be defined for minor and trace elements.

Regardless of the instrumentation used on an in situ investigation of the lunar farside, one of the main challenges faced by farside exploration is the ability to communicate data back to Earth. To mitigate this, the Chang'E-4 landed mission to the lunar SPA basin relies on the Queqiao relay satellite, which orbits a Lagrange point, to relay data from the lunar farside with a direct line of sight to Earth (Zhang et al. 2020). Further technology has been proposed as part of the Lunar Gateway under the NASA Artemis program, which would produce an orbiting platform in cislunar space and could act as a communications relay satellite as well (Smith et al. 2020).

3.2. Developing Technology

Significant time and research dollars have been invested in developing advanced in situ analytical techniques for emerging planetary science objectives. Novel technologies designed to achieve enhanced performance metrics, such as lower limits of detection, and/or reduced resource requirements, such as power consumption, may enable measurements of trace element abundances and isotopic ratios previously considered inaccessible for landed missions. Particular interest centers on the advancement of instrumentation capable of establishing chronological constraints via K-Ar and Rb-Sr radiometric dating. The K-Ar Laser Experiment (KArLE) uses an LIBS instrument to measure the K abundance of a sample and a quadrupole mass analyzer to determine the absolute amount of radiogenic ^{40}Ar released during laser processing (Cohen et al. 2014); the analysis of other noble gas isotopes, including $^{36,38}Ar$ and $^{20,21,22}Ne$, provides constraints on exposure ages (Farley et al. 2014). The Rb-Sr isotope system can be accessed
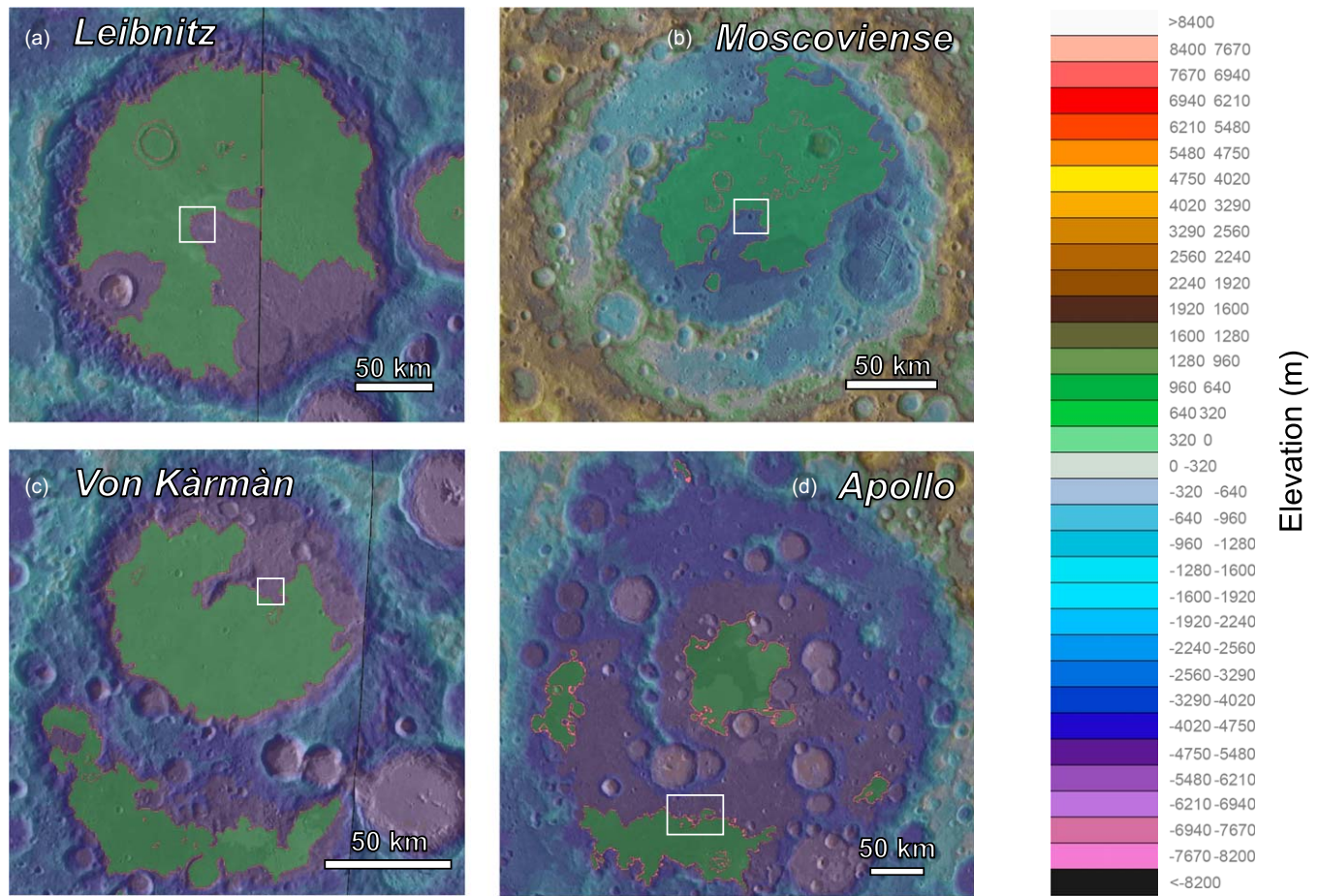
Figure 6. Composite maps of four potential landing sites selected at (a) Leibnitz, (b) Moscoviense, (c) Von Kármán, and (d) Apollo craters. Images are compiled using the *LRO Quickmap* mapping tool, with topography data overlaid from the LRO LOLA instrument and topography scale bar to the right. Locations of mare basalt units are infilled with green, and the area targeted as the primary landing site is marked by a white square.

Table 2
Assessment of Four Landing Sites Proposed for Trace Element Analyses

	Moscoviense	Apollo	Von Kármán	Liebnitz
Coordinates (lat)	23°32–24°7	−38°62 to −40°91	−43°32 to −44°33	−37°94 to −39°16
Coordinates (long)	146°83–148°00	−149°51 to −151°53	176°81–177°84	−−178°26 to −179°79
Crustal thickness	<500 m	<1 km–~5 km	10–20 km	5–10 km
Slope	2°–7°	<1°–5°	1°–10°	<1°–2°
Temperature anomaly	+5 K	+2 K to +3 K	−3 K to +3 K	−3 K to +3 K
Olivine (wt.%)	2.5–7.5	7.5–12.5	2.5–5	<2.5–7.5
Orthopyroxene (wt.%)	21–28	28–35	21-28	21–35
Clinopyroxene (wt.%)	25–30	7–14	14–28	14–28
Plagioclase (wt.%)	10–15	30–50	15–25	25–40
FeO (wt.%)	12.5–15	10–15	10–12.5	10–15
TiO$_2$ (wt.%)	2–3	<2	<2–3	<2
Stratigraphic age	Nectarian	Pre-Nectarian	Pre-Imbrium	Pre-Nectarian

Note. Data for each site taken from LRO—Quickmap mapping tool. Crustal thickness measurements from GRAIL mission, slope measurements from LRO—LOLA instrument, temperature anomalies from LRO—DIVINER instrument, mineralogy from SELENE/Kaguya measurements, and TiO$_2$ measurements from LROC—WAC 321/415 nm band ratio.

through the Chemistry, Organics, and Dating EXperiment (CODEX), which relies on multiple laser systems that generate light at specific wavelengths to desorb and resonantly ionize Rb and Sr separately, avoiding the isobaric interference between ^{87}Rb and ^{87}Sr during mass analysis (Anderson et al. 2020). Both of these investigations have demonstrated the ability to meet or exceed the NASA goal of determining absolute ages of

planetary materials with a minimum precision better than ± 5% (2σ; 2015 ROADMAP).

The progressive development of high-powered laser systems and a variety of mass analyzers that can be interfaced to such sources indicates that chemical imaging of trace elements and isotopic ratios is within the reach of near-term mission opportunities. Laser desorption/ablation mass spectrometry
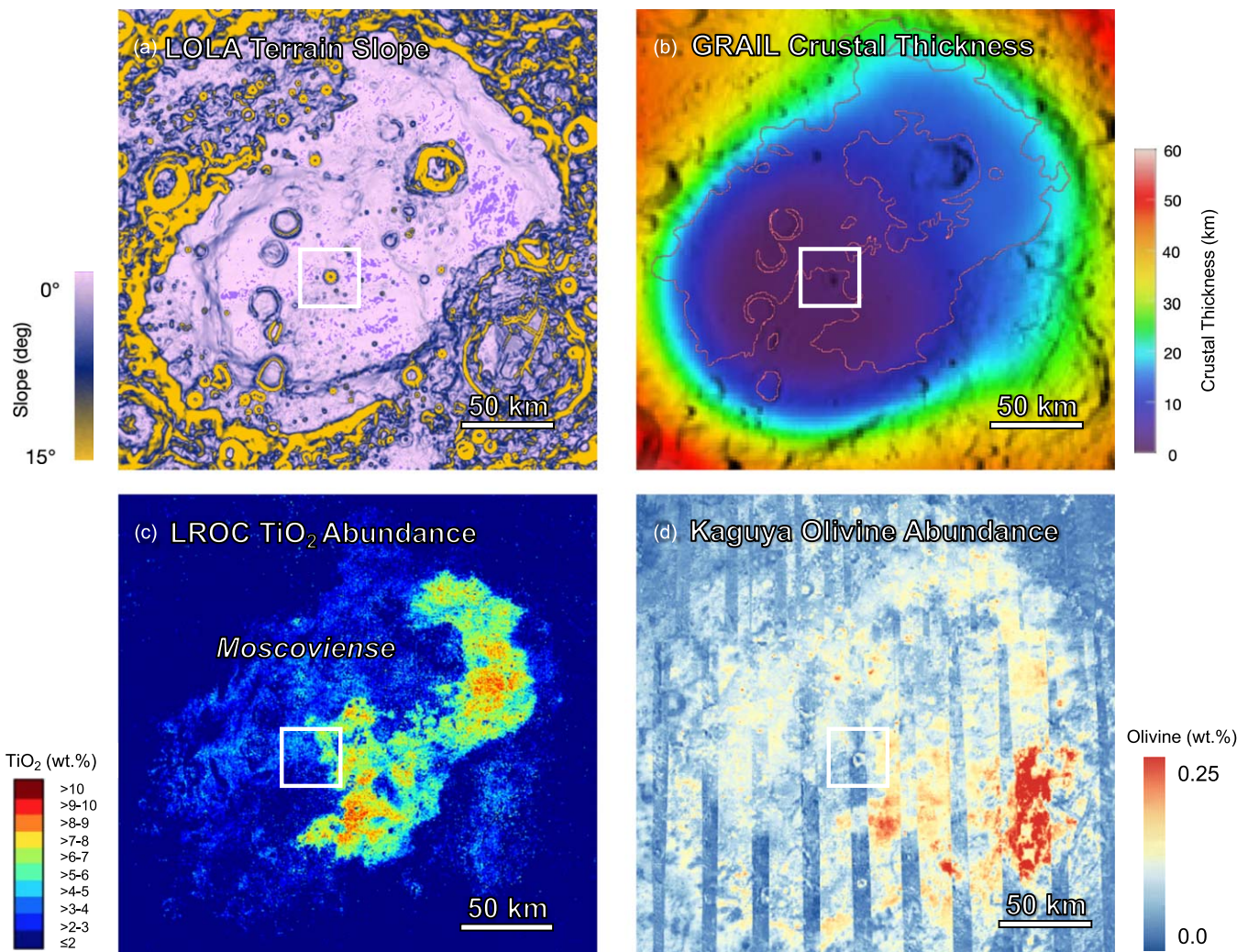
Figure 7. (a) Slope, (b) crustal thickness, (c) TiO$_2$ abundance, and (d) olivine abundance maps of Moscoviense crater. The white square identifies the proposed landing site.

techniques, as enabled by miniaturized instruments that have a direct path to a spaceflight, have been shown to deliver 2D chemical maps of planetary analog samples (Neuland et al. 2014), 3D depth profiles of solid substrates (Grimaudo et al. 2015), and contemporaneous measurements of organic compounds and their host matrix (Arevalo et al. 2018). However, in the laboratory, inductively coupled plasma mass spectrometer (ICPMS) systems serve as the gold standard for measuring trace and ultratrace element abundances down to sub-ppbw levels in natural samples. A commercial ICPMS typically requires between 1200 and 1600 W and 14–18 L/min Ar gas to generate a high-temperature plasma that effectively atomizes and ionizes geologic materials introduced by laser ablation (e.g., Niu & Houk 1996). However, recent work has demonstrated the feasibility of using less power (<25 W) and reduced gas flow rates (<0.2 L min^{-1}) to produce a plasma capable of atomizing and ionizing geologic material at similar efficiencies to a commercial instrument (Figure 5; Farcy et al. 2020b), albeit with higher detection limits due to a limited capacity to support mass loading. Thus, in the near future emerging technologies may enable measurements of trace elements and isotopic systems with lower detection thresholds,

spatially resolved sampling, and higher precision/accuracy to further support the science objectives outlined in this work.

4. Landing Site Analysis

The goal of the proposed investigation is to understand better the petrology and formation history of the BSM by characterizing the composition of and placing temporal constraints on the evolution of the lunar farside. Achieving the science goals outlined above will require trace element analyses of lithologies representing the upper and lower mantle sources of mare. To maximize science return, specific landing sites that would provide the most valuable samples for this investigation have been identified. The SPA basin was formed by a large impactor on the lunar farside resulting in melt that samples down to a depth of 400–600 km. Later, this melt crystallized into norite and troctolite in the valley floors of impact basins (Hurwitz & Kring 2014). While the impact model does predict differentiation of the melt sheet, a norite or troctolite quenched cap is predicted to form prior to differentiation, meaning that the unit exposed to the surface does represent the bulk composition of the impact melt. This impact melt and subsequent quench cap resulted in anomalously thin crust in impact basins, ranging in thickness from <1 to 10 km. Thin crust
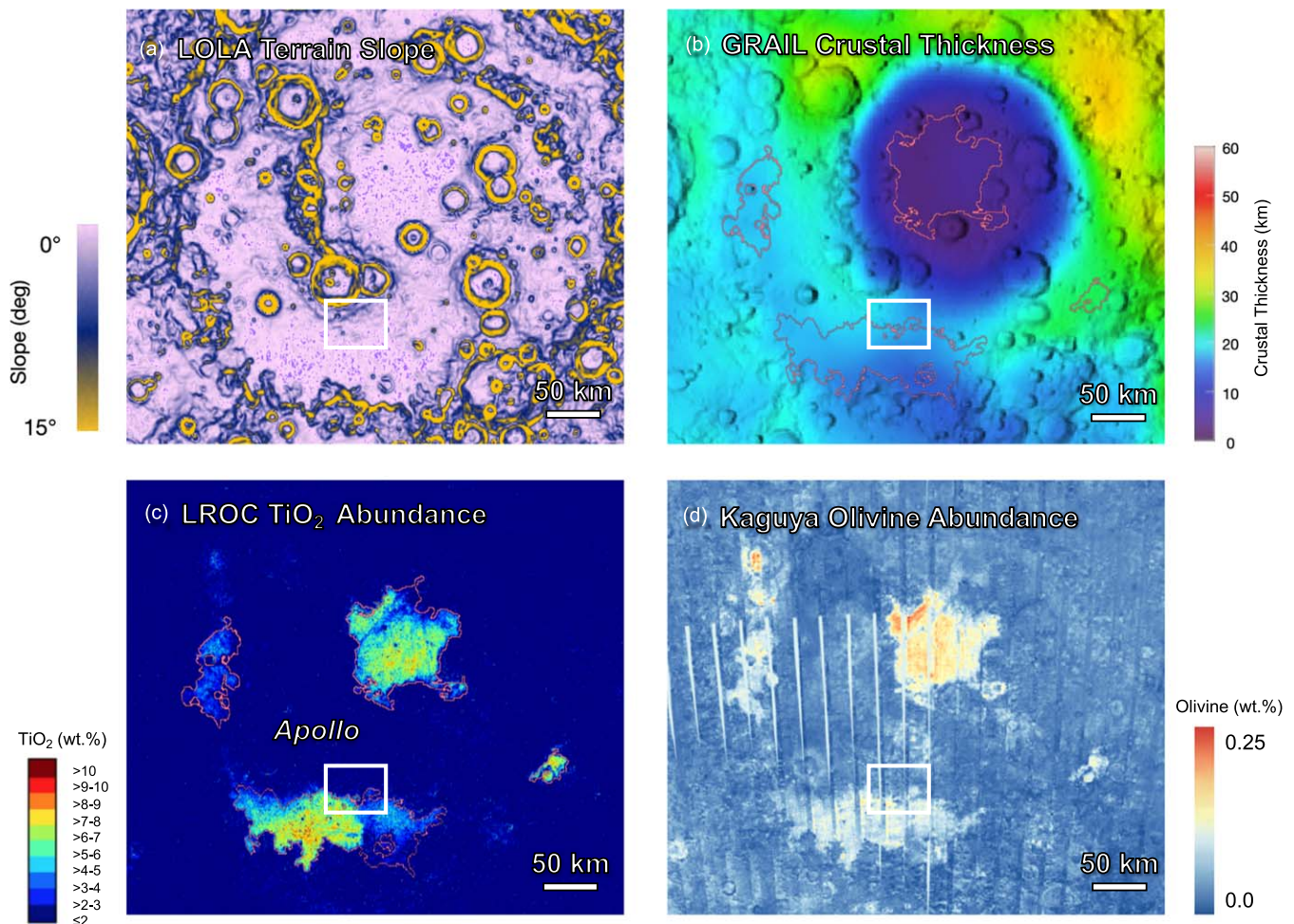
Figure 8. (a) Slope, (b) crustal thickness, (c) TiO$_2$ abundance, and (d) olivine abundance maps of Apollo crater. The white square identifies the proposed landing site.

resulting from impacts preferentially allows melt to puncture through the crust, causing later mare basalts to accumulate in impact basins (Wilson & Head 1981). Thus, impact basins containing both norite/troctolite impact melts and later mare emplacement are ideal candidates for the outlined analyses.

We assessed potential landing sites on the lunar farside using orbital-based spectroscopic and geophysical measurements, with data overlays compiled using the *LRO Quickmap* mapping tool. TiO$_2$ measurements are derived from the Lunar Reconnaissance Orbiter Camera (LROC) Wide-Angle Camera (WAC), using 321/415 nm band ratios; crustal thickness is derived from the GRAIL mission Bougier gravity anomaly map; and slope measurements are generated using the LRO LOLA laser altimeter. Surficial mineralogy is derived from the Kaguya Mineral Mapper instrument, although some spectral bands have been shown to misidentify lithologies. Specifically, the 1 μm absorption band associated with olivine is also observed in volcanic glass; thus, pyroclastic deposits have been previously misidentified as olivine (Moriarty & Petro 2020). Despite this, the Kaguya Mineral Mapper is a powerful tool for detecting the lithologies targeted for this mission concept.

While impact melt is one of the lithologies targeted for these analyses, the exposed impact melts on the crater floors may prove to be more complicated. Impact gardening may overlay the crater floor with ejecta from surrounding craters, obscuring the exposed basement rock. To mitigate this complication, other mission concepts have suggested sampling the central

uplift of the crater, which would not be obscured with regolith (Runyon et al. 2020). Thus, the majority of our landing sites have been chosen to be close to the central uplift of the crater to avoid accumulated regolith. These areas are also close to mare deposits, allowing access to multiple target lithologies.

Landing site analyses were carried out to minimize mission risk and maximize science return. Sites were selected based on four main criteria:

1. Low crustal thickness anomalies.
2. Norite or troctolite exposed on the impact basin floor.
3. Later-stage mare deposits observed within the impact basin.
4. Minimal landing site hazards (e.g., slope, temperature, rock/fine fraction).

Based on these criteria, we have identified Moscoviense, Apollo, Von Kármán, and Leibnitz craters as potential landing sites (Figure 6). A mobile platform such as a rover or a secondary launch vehicle could sample both basement impact melt and mare deposits. A summary of each landing site analysis is found in Table 2.

4.1. Moscoviense Crater

Moscoviense is a Nectarian-age impact basin with a series of concentric ring impact structures and multiple Imbrium- and Erasthothenian-aged mare units (Thaisen et al. 2011). Moscoviense
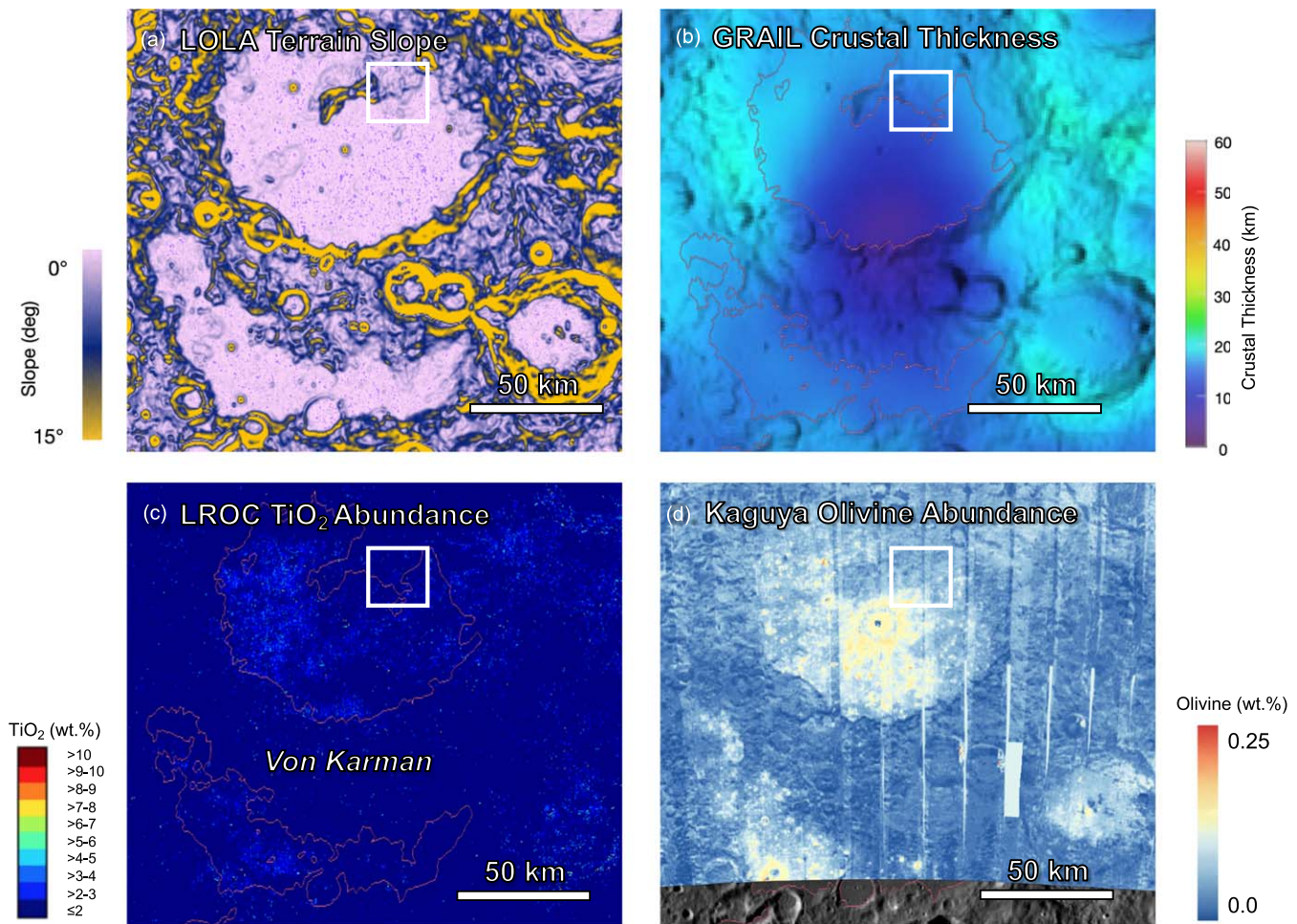
Figure 9. (a) Slope, (b) crustal thickness, (c) TiO$_2$ abundance, and (d) olivine abundance maps of Von Kármán crater. The white square identifies the proposed landing site.

is the northernmost impact basin considered as a landing site on the lunar farside, and thus not associated with the impact formation of the SPA basin. Despite the impact structures, the valley of the basin contains limited topographical features and near-zero slope, providing a relatively hazard-free terrain to traverse. This landing site could provide a window into the lunar mantle, as the crust beneath Moscoviense is the thinnest part of the lunar surface, with crustal thickness estimates of 400–500 m, based on measurements from the Kaguya and GRAIL missions (Ishihara et al. 2009; Wieczorek et al. 2013).

TiO$_2$ measurements and crater counting estimates of the later-emplaced mare basalts show a time and compositional discrepancy between basalt units, with older mare units to the northwest having a distinctly lower TiO$_2$ abundance (<2 wt.%) and younger units to the east having a significantly higher (5–10 wt.%) TiO$_2$ abundance (Figure 7). AMAs have been estimated for different units in Moscoviense, with the western low-TiO$_2$ basalts (3.5 Ga) forming ~1 Ga earlier than the high TiO$_2$ eastern mare (2.5 Ga; Morota et al. 2009). However, subsequent crater counting analysis of the lunar farside indicated that mare volcanism was active over a longer period than previously estimated, thus requiring further chronological constraints (Pasckert et al. 2015). Differences in composition and age indicate that the mare emplaced in Moscoviense reflects multiple mantle source regions, allowing a multifaceted

investigation into the composition and formation history of the lunar mantle.

4.2. Apollo Crater

Apollo crater, the largest impact structure in the SPA basin, is pre-Nectarian in age. The SPA basin is an important target for understanding lunar history, as crater ages from this region can help explain the timing and intensity of the impactor flux during this period of time, enabling a critical evaluation of the putative LHB. Further, the region itself represents portions of the lunar upper mantle exposed through impact melts; the valley floor of Apollo crater represents one such exposure. Norite and troctolite in the crater floor likely formed as impact melt, and the low crustal thickness (~5 km) makes Apollo an ideal candidate for measuring the composition of the lunar upper mantle and constraining the impact age of the SPA basin.

Apollo crater also contains up to eight distinct mare basalt units, separated spatially, chronologically, and compositionally (Figure 8). The AMA estimates for the basalt units in Apollo basin vary. The two southern mare units separated by high and low TiO$_2$ abundance may have formed within 150 Myr of each other (3.31 and 3.45 Ga; Pasckert et al. 2018), or by as much as 1 Ga (2.44 Ga; Haruyama et al. 2009). Thus, in situ chronology can help resolve the discrepancy of the timing of farside mare basalt emplacement and better calibrate the crater counting
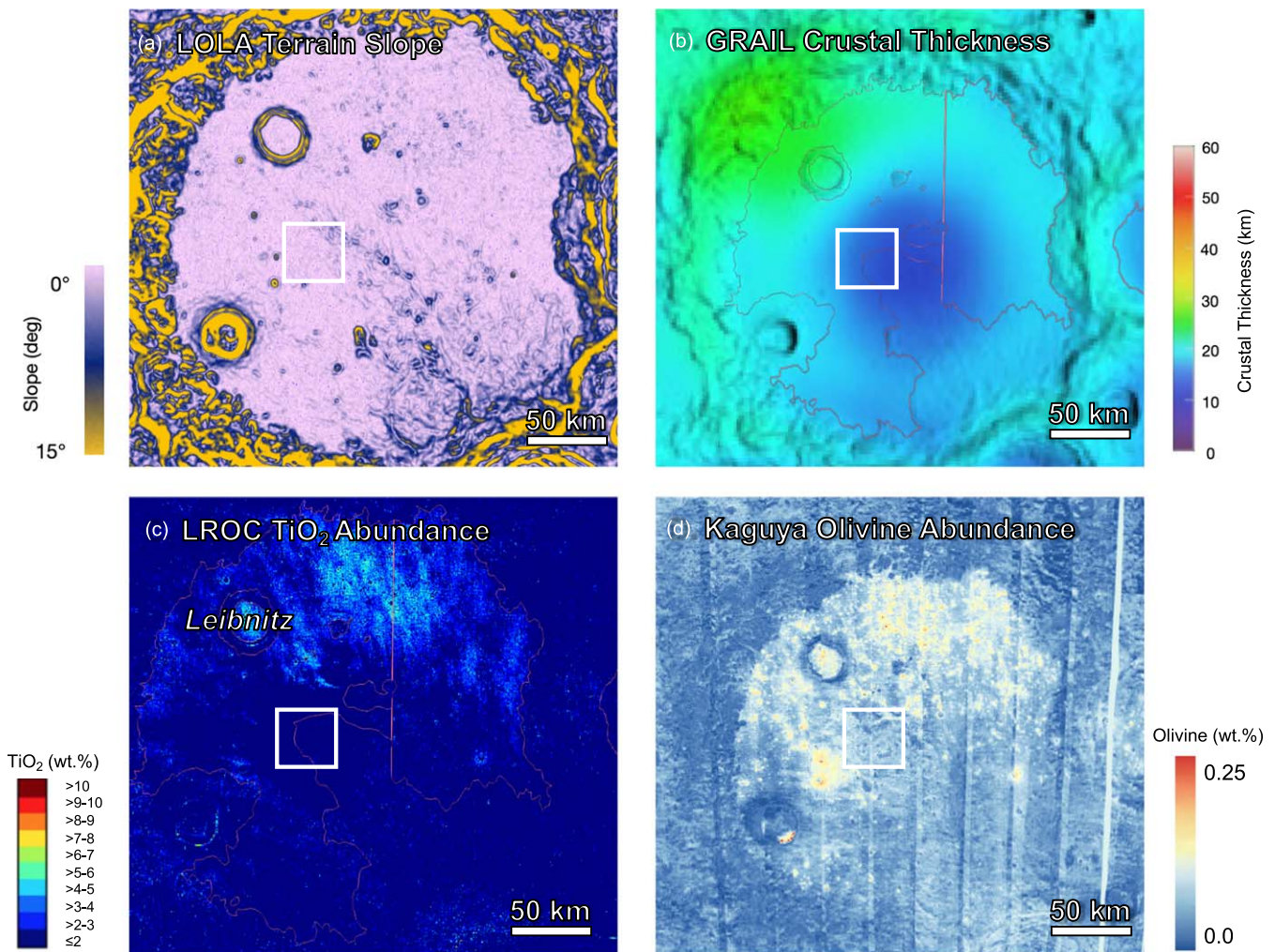
Figure 10. (a) Slope, (b) crustal thickness, (c) TiO$_2$ abundance, and (d) olivine abundance maps of Leibnitz crater. The white square identifies the proposed landing site.

record for the farside SPA basin. Similar to Moscoviense, mare units to the southwest show compositional differences, with older units having lower TiO$_2$ than younger units, indicating a shift in the mantle source of mare basalts in Apollo crater as well.

4.3. Von Kármán Crater

Von Kármán crater is pre-Nectarian in age, lies to the southwest of Leibnitz crater, and is compositionally similar in both basement rock lithology and later emplacement of mare basalts. AMA estimates for Von Kármán crater are ~4.2 Ga, with subsequent mare basalts and ejecta layers from Finsen craters dating to 3.1–3.5 Ga (Lu et al. 2021). Von Kármán is composed of multiple ring structures with mare units infilling the ringed units. Measurements from the M^3 spacecraft on the Chandryaan-1 mission show that the area surrounding Leibnitz and Von Kármán craters contains abundant pyroxene (Moriarty & Pieters 2018), mainly Ca- and Fe-rich pyroxene in the north and northwest region of the SPA basin. The northernmost rim of the crater is characterized by norite and troctolite basement rock, with mare basalt infilling the majority of the basin. The northern rim is also marked by multiple smaller craters and slightly sloped areas of 2°–7°. Crustal thickness measurements show the northern rim with 15–20 km crustal thickness, but a

crustal thickness <5 km on the southern portion of the largest mare unit (Figure 9).

Von Kármán crater is also the landing site of the Chang'E-4 Yutu rover. The formation and regolith stratigraphy of Von Kármán crater have been observed by this mission, revealing the composition and sources of the material. In situ near-IR measurements show that the regolith is mainly olivine norite, reflective of the lunar lower crust (Lin et al. 2020). The regolith material is likely sourced from surrounding craters, namely, Finsen and Leibnitz, obscuring the mare infill in the crater floor (Lin et al. 2020; Zhang et al. 2020). Here, the proposed landing site for Von Kármán targets the edge of a topographical high, which would minimize the accumulation of regolith while optimizing exposed impact melt rock (Runyon et al. 2020).

4.4. Leibnitz Crater

Leibnitz crater at the northwest corner of the SPA basin is pre-Imbrium to post-Nectarian, with basalt units possibly forming at 3.4–3.7 Ga (Pasckert et al. 2018). Leibnitz crater has a larger amount of mare infill compared to Apollo and Moscoviense, filling in the majority of the crater floor, which itself is noritic in composition (Borst et al. 2012; Hurwitz & Kring 2014). The central portion of the crater has a thin crust (5–10 km), meaning that the noritic basement is likely

homogenized upper mantle after an impact melt (Figure 10). This area is relatively flat with few large boulders, minimizing operational hazards of a landed mission. UV/VIS spectroscopy shows excavated gabbroic ejecta inside the basin from nearby Finsen crater, possibly allowing the analyses of material from multiple impacts (Borst et al. 2012).

The landing sites identified provide a window into the lunar farside interior, with impacts producing thin crust and possibly exposing the upper mantle, and later basaltic melts reflecting previously unsampled mare source regions. In situ chemical analyses of trace elements in rocks representing specific processes and eras in lunar history can be a low-risk, high-reward strategy for future lunar science.

5. Conclusions

Here, as with previous missions, trace elements are useful for characterizing the range of dynamic processes that have shaped the evolution of the Moon and other planets. Heritage instruments and emerging technologies allow for the measurements of elemental abundances to lower limits of detection than realized historically. These technologies can be used to reevaluate evolutionary models of the Moon, based on the characterization of materials derived from specific landing sites on its farside. In addition, they provide a resource tool for defining the distribution of valuable trace elements in local surface materials. A landed in situ investigation of lunar farside lithologies could provide science return for less risk than a crewed mission or sample return and should be one of the major focus areas for future landed lunar science.

ORCID iDs

Benjamin Farcy https://orcid.org/0000-0001-5159-6551
Ricardo Arevalo, Jr. https://orcid.org/0000-0002-0558-5090
William F. McDonough https://orcid.org/0000-0001-9154-3673

References

Allwood, A., Clark, B., Flannery, D., et al. 2015, in 2015 IEEE Aerospace Conf. (Piscataway, NJ: IEEE), 1
Anderson, S., Levine, J., & Whitaker, T. 2020, P&SS, 191, 105007
Arai, T., Takeda, H., Yamaguchi, A., & Ohtake, M. 2008, EP&S, 60, 433
Arevalo, R., & McDonough, W. F. 2010, ChGeo, 271, 70
Arevalo, R., McDonough, W. F., & Luong, M. 2009, E&PSL, 278, 361
Arevalo, R., Selliez, L., Briois, C., et al. 2018, RCMS, 32, 1875
Barboni, M., Boehnke, P., Keller, B., et al. 2017, SciA, 3, 2365
Biemann, K., Oro, J., Toulmin, P., III, et al. 1977, JGR, 82, 4641
Blake, D., Vaniman, D., Achilles, C., et al. 2012, SSRv, 170, 341
Borg, L. E., Cassata, W. S., Wimpenny, J., Gaffney, A. M., & Shearer, C. K. 2020, GeCoA, 290, 312
Borg, L. E., Gaffney, A. M., & Shearer, C. K. 2015, M&PS, 50, 715
Borst, A., Foing, B., Davies, G., & Van Westrenen, W. 2012, P&SS, 68, 76
Bottke, W. F., & Norman, M. D. 2017, AREPS, 45, 619
Boukaré, C.-E., Parmentier, E., & Parman, S. 2018, E&PSL, 491, 216
Campbell, J. 2012, NIMPB, 288, 102
Canup, R. M., Visscher, C., Salmon, J., & Fegley, B., Jr. 2015, NatGe, 8, 918
Cassanelli, J. P., & Head, J. W. 2016, GeoRL, 43, 11,156
Charlier, B., Grove, T. L., Namur, O., & Holtz, F. 2018, GeCoA, 234, 50
Clark, B. C., Baird, A., Rose, H. J., et al. 1977, JGR, 82, 4577
Cohen, B. A., Miller, J. S., Li, Z.-H., Swindle, T. D., & French, R. A. 2014, Geostand. Geoanal. Res., 38, 421
Cohen, B. A., Young, K. E., Zellner, N. E., et al. 2021, PSJ, in press (arXiv:2101.01131)
Combs, L. M., Udry, A., Howarth, G. H., et al. 2019, GeCoA, 266, 435
Connelly, J., & Bizzarro, M. 2016, E&PSL, 452, 36
Coogan, L., Saunders, A., & Wilson, R. 2014, ChGeo, 368, 1
Crites, S. T., & Lucey, P. G. 2015, AmMin, 100, 973
Curran, N. M., Joy, K., Snape, J., et al. 2019, M&PS, 54, 1401
Davis, A. M. 2006, Meteorites and the Early Solar System II, Vol. 1 (Tucson, AZ: Univ. Arizona Press), 295
Davis, F. A., Humayun, M., Hirschmann, M. M., & Cooper, R. S. 2013, GeCoA, 104, 232
Day, J. M., & Moynier, F. 2014, RSPTA, 372, 20130259
De Hoog, J. C., Gall, L., & Cornell, D. H. 2010, ChGeo, 270, 196
Delano, J. W. 1986, JGR, 91, 201
Dhingra, D., Pieters, C. M., Head, J. W., & Isaacson, P. J. 2013, GeoRL, 40, 1043
Dickinson, T., Taylor, G., Keil, K., & Bild, R. 1989, LPSC, 19, 189
Elardo, S. M., Laneuville, M., McCubbin, F. M., & Shearer, C. K. 2020, NatGe, 13, 339
Elkins-Tanton, L. T., Burgess, S., & Yin, Q.-Z. 2011, E&PSL, 304, 326
Evans, A. 2019, LPSC, 50, 2733
Farcy, B., Arevalo, R., & McDonough, W. 2020a, JGRB, 125, 20245
Farcy, B., Arevalo, R., Taghioskoui, M., et al. 2020b, J. Anal. At. Spectrom., 35, 2740
Farley, K. A., Malespin, C., Mahaffy, P., et al. 2014, Sci, 343, 1247166
Filiberto, J., Musselwhite, D. S., Gross, J., et al. 2010, M&PS, 45, 1258
Foley, C., Economou, T., & Clayton, R. 2001, LPSC, 32, 1979
Gagnepain-Beyneix, J., Lognonné, P., Chenet, H., Lombardi, D., & Spohn, T. 2006, PEPI, 159, 140
Garrick-Bethell, I., Nimmo, F., & Wieczorek, M. A. 2010, Sci, 330, 949
Gillis, J. J., Jolliff, B. L., & Korotev, R. L. 2004, GeCoA, 68, 3791
Goesmann, F., Brinckerhoff, W. B., Raulin, F., et al. 2017, AsBio, 17, 655
Grimaudo, V., Moreno-García, P., Riedo, A., et al. 2015, AnaCh, 87, 2037
Gurenko, A. A., Sobolev, A. V., Hoernle, K. A., Hauff, F., & Schmincke, H.-U. 2009, E&PSL, 277, 514
Hagerty, J. J., Lawrence, D., & Hawke, B. 2011, JGRE, 116, E06001
Hagerty, J. J., Shearer, C. K., & Vaniman, D. T. 2006, GeCoA, 70, 3457
Hartmann, W. K. 2019, Geosc, 9, 285
Haruyama, J., Ohtake, M., Matsunaga, T., et al. 2009, Sci, 323, 905
He, D., Lee, C.-T. A., Yu, X., & Farner, M. 2019, GGG, 20, 4472
Head, J. W., & Wilson, L. 1992, GeCoA, 56, 2155
Herzberg, C., & Asimow, P. 2015, GGG, 16, 563
Hess, P. C., & Parmentier, E. 1995, E&PSL, 134, 501
Hurwitz, D. M., & Kring, D. A. 2014, JGRE, 119, 1110
Ishihara, Y., Goossens, S., Matsumoto, K., et al. 2009, GeoRL, 36, L19202
Jafar, A.-H., & Pentecost, A. 2001, JGR, 106, 14691
Jolliff, B. L., Gillis, J. J., Haskin, L. A., Korotev, R. L., & Wieczorek, M. A. 2000, JGR, 105, 4197
Jones, J. H., & Palme, H. 2000, Origin of the Earth and Moon, Vol. 30 (Tucson, AZ: Univ. Arizona Press), 197
Kaula, W. M., Schubert, G., Lingenfelter, R. E., Sjogren, W., & Wollenhaupt, W. 1974, LPSC, 5, 3049
Klingelhöfer, G., Brückner, J., D'uston, C., Gellert, R., & Rieder, R. 2007, SSRv, 128, 383
Kuskov, O., & Kronrod, V. 1998, PEPI, 107, 285
Laneuville, M., Taylor, J., & Wieczorek, M. 2018, JGRE, 123, 3144
Laneuville, M., Wieczorek, M., Breuer, D., & Tosi, N. 2013, JGRE, 118, 1435
Lassiter, J. C. 2004, GGG, 5, Q11012
Le Roux, V., Dasgupta, R., & Lee, C.-T. 2011, E&PSL, 307, 395
Lin, H., He, Z., Yang, W., et al. 2020, Natl. Sci. Rev., 7, 913
Lodders, K. 2020, The Oxford Research Encyclopedia of Planetary Science (Oxford: Oxford Univ. Press)
Longhi, J. 1992, GeCoA, 56, 2235
Longhi, J. 1993, LPSC, 24, 895
Longhi, J. 1995, GeCoA, 59, 2375
Longhi, J. 2006, GeCoA, 70, 5919
Longhi, J., Durand, S. R., & Walker, D. 2010, GeCoA, 74, 784
Lu, Y., Wu, Y., Michael, G. G., et al. 2021, Icar, 354, 114086
Mahaffy, P. R., Webster, C. R., Cabane, M., et al. 2012, SSRv, 170, 401
Maltese, A., & Mezger, K. 2020, GeCoA, 271, 179
Matzen, A. K., Wood, B. J., Baker, M. B., & Stolper, E. M. 2017, NatGe, 10, 530
Maurice, M., Tosi, N., Schwinger, S., Breuer, D., & Kleine, T. 2020, SciA, 6, 8949
McDonough, W. F., & Sun, S.-S. 1995, ChGeo, 120, 223
Melosh, H., Kendall, J., Horgan, B., et al. 2017, Geo, 45, 1063
Miljković, K., Wieczorek, M. A., Collins, G. S., et al. 2015, E&PSL, 409, 243
Morgan, J. W., Hertogen, J., & Anders, E. 1978, M&P, 18, 465

Moriarty, D., & Petro, N. 2020, LPSC, 50, 2660
Moriarty, D., Pieters, C., & Isaacson, P. 2013, JGRE, 118, 2310
Moriarty, D., III, & Pieters, C. 2018, JGRE, 123, 729
Moriarty, D., III, Watkins, R., Valencia, S., et al. 2020, JGRE, 126, 6589
Morota, T., Haruyama, J., Honda, C., et al. 2009, GeoRL, 36, L21202
Neal, C. R. 2001, JGR, 106, 27865
Nekvasil, H., Dondolini, A., Horn, J., et al. 2004, JPet, 45, 693
Nekvasil, H., Filiberto, J., McCubbin, F. M., & Lindsley, D. H. 2007, M&PS, 42, 979
Nemchin, A., Timms, N., Pidgeon, R., et al. 2009, NatGe, 2, 133
Neuland, M. B., Meyer, S., Mezger, K., et al. 2014, P&SS, 101, 196
Niu, H., & Houk, R. 1996, AcSpe, 51, 779
Ohtake, M., Matsunaga, T., Haruyama, J., et al. 2009, Natur, 461, 236
Ohtake, M., Takeda, H., Matsunaga, T., et al. 2012, NatGe, 5, 384
Parmentier, E., Zhong, S., & Zuber, M. 2002, E&PSL, 201, 473
Pasckert, J. H., Hiesinger, H., & van der Bogert, C. H. 2015, Icar, 257, 336
Pasckert, J. H., Hiesinger, H., & van der Bogert, C. H. 2018, Icar, 299, 538
Patterson, J. H., Franzgrote, E. J., Turkevich, A. L., et al. 1969, JGR, 74, 6120
Prettyman, T., Hagerty, J., Elphic, R., et al. 2006, JGRE, 111, E12007
Putirka, K. 1999, JGR, 104, 2817
Putirka, K., Perfit, M., Ryerson, F., & Jackson, M. G. 2007, ChGeo, 241, 177
Rapp, J., & Draper, D. 2018, M&PS, 53, 1432
Rieder, R., Gellert, R., Brückner, J., et al. 2003, JGRE, 108, 8066
Roeder, P., & Emslie, R. 1970, CoMP, 29, 275
Runyon, K., Moriarty, D., III, Denevi, B., et al. 2020, JGRE, 125, e06024
Shearer, C., Hess, P., Wieczorek, M., et al. 2006, RvMG, 60, 365
Shearer, C. K., & Papike, J. 2005, GeCoA, 69, 3445
Shirley, D., & Wasson, J. 1982, LPSC, 12, 965
Smith, M., Craig, D., Herrmann, N., et al. 2020, in 2020 IEEE Aerospace Conf. (Piscataway, NJ: IEEE), 1
Snyder, G. A., Taylor, L. A., & Neal, C. R. 1992, GeCoA, 56, 3809
Sobolev, A. V., Hofmann, A. W., Sobolev, S. V., & Nikogosian, I. K. 2005, Natur, 434, 590
Solomon, S. C., & Longhi, J. 1977, LPSC, 8, 583
Stegman, D. R., Jellinek, A. M., Zatman, S. A., Baumgardner, J. R., & Richards, M. A. 2003, Natur, 421, 143
Surkov, Y. A., Barsukov, V., Moskalyeva, L., Kharyukova, V., & Kemurdzhian, A. 1984, JGRB, 89, B393
Tatsumoto, M., Knight, R. J., & Allegre, C. J. 1973, Sci, 180, 1279
Tatsumoto, M., Premo, W. R., & Unruh, D. M. 1987, JGR, 92, E361
Taylor, J., & Wieczorek, M. 2014, RSPTA, 372, 20130242
Taylor, S. R. 1982, Planetary Science: A Lunar Perspective (Houston, TX: Lunar and Planetary Inst.)
Taylor, S. R. 1999, in The Moon in Encyclopedia of the Solar System, ed. P. R. Weissman, L.-A. McFadden, & T. V. Johnson (San Diego, CA: Academic)
Taylor, S. R., Taylor, J., & Taylor, L. A. 2006, GeCoA, 70, 5904
Thaisen, K. G., Head, J. W., Taylor, L. A., et al. 2011, JGRE, 116, E00G07
Thiemens, M. M., Sprung, P., Fonseca, R. O., Leitzke, F. P., & Münker, C. 2019, NatGe, 12, 696
Vaughan, W. M., & Head, J. W. 2014, P&SS, 91, 101
Wan, Z., Coogan, L. A., & Canil, D. 2008, AmMin, 93, 1142
Wang, Z., & Gaetani, G. A. 2008, CoMP, 156, 661
Wänke, H., & Dreibus, G. 1982, Tidal Friction and the Earth's Rotation II (Berlin: Springer), 322
Warren, P., & Taylor, G. 2014, TrGeo, 1, 559
Warren, P. H. 1985, AREPS, 13, 201
Warren, P. H. 2005, M&PS, 40, 477
Wieczorek, M. A., Jolliff, B. L., Khan, A., et al. 2006, RvMG, 60, 221
Wieczorek, M. A., Neumann, G. A., Nimmo, F., et al. 2013, Sci, 339, 671
Wiens, R., Maurice, S., Lasue, J., et al. 2013, AcSpe, 82, 1
Wiens, R., Newell, R., Clegg, S., et al. 2017, LPSC, 48, 2600
Wiens, R. C., Maurice, S., Barraclough, B., et al. 2012, SSRv, 170, 167
Wilson, L., & Head, J. W. 1981, JGR, 86, 2971
Wolf, R., & Anders, E. 1980, GeCoA, 44, 2111
Wood, J. A., Dickey, J. S., Jr., Marvin, U. B., & Powell, B. 1970, GeCAS, 1, 965
Yamamoto, S., Nakamura, R., Matsunaga, T., et al. 2012, Icar, 218, 331
Yang, S., Humayun, M., & Salters, V. J. 2020, SciA, 6, 2923
Zhang, J., Zhou, B., Lin, Y., et al. 2020, NatAs, 5, 1
Zhong, S., Parmentier, E., & Zuber, M. T. 2000, E&PSL, 177, 131
Zhu, M.-H., Ma, T., Chang, J., et al. 2011, SCPMA, 54, 2083